AD-A189 475 SPECTRAL MULTIGRID METHODS FOR THE SOLUTION OF HOMOGENEOUS TURBULENCE PRO.. (U) INSTITUTE FOR COMPUTER APPLICATIONS IN SCIENCE AND ENGINEERIN.. 1/1

UNCLASSIFIED G ERLEBACHER ET AL. JUL 87 ICASE-87-45 F/G 12/1 NL

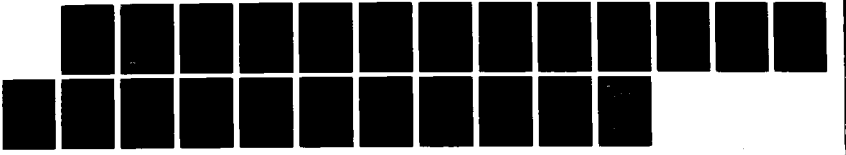

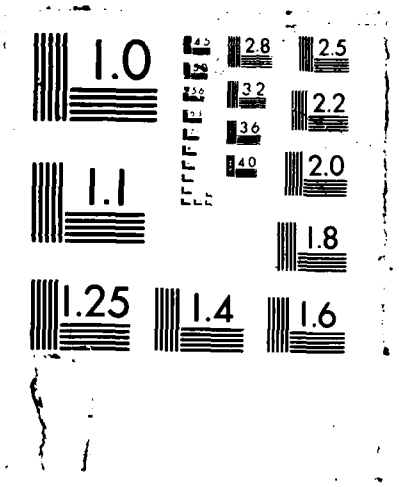
1.0
1.1
1.25
1.4
1.6
1.8
2.0
2.2
2.5
2.8
3.2
3.6
4.0

NASA Contractor Report 178341

ICASE REPORT NO. 87-45

ICASE

SPECTRAL MULTIGRID METHODS FOR THE SOLUTION OF HOMOGENEOUS TURBULENCE PROBLEMS

G. Erlebacher

T. A. Zang

M. Y. Hussaini

Contract No. NAS1-18107
July 1987

INSTITUTE FOR COMPUTER APPLICATIONS IN SCIENCE AND ENGINEERING
NASA Langley Research Center, Hampton, Virginia 23665

Operated by the Universities Space Research Association

National Aeronautics and
Space Administration

Langley Research Center
Hampton, Virginia 23665

SPECTRAL MULTIGRID METHODS FOR THE SOLUTION OF HOMOGENEOUS TURBULENCE PROBLEMS

G. Erlebacher and T. A. Zang
NASA Langley Research Center

M.Y. Hussaini*
Institute for Computer Applications in Science and Engineering

New three-dimensional spectral multigrid algorithms are analyzed and implemented to solve the variable coefficient Helmholtz equation. Periodicity is assumed in all three directions which leads to a Fourier collocation representation. Convergence rates are theoretically predicted and confirmed through numerical tests. Residual averaging results in a spectral radius of 0.2 for the variable coefficient Poisson equation. In general, non-stationary Richardson must be used for the Helmholtz equation. The algorithms developed are applied to the large-eddy simulation of incompressible isotropic turbulence.

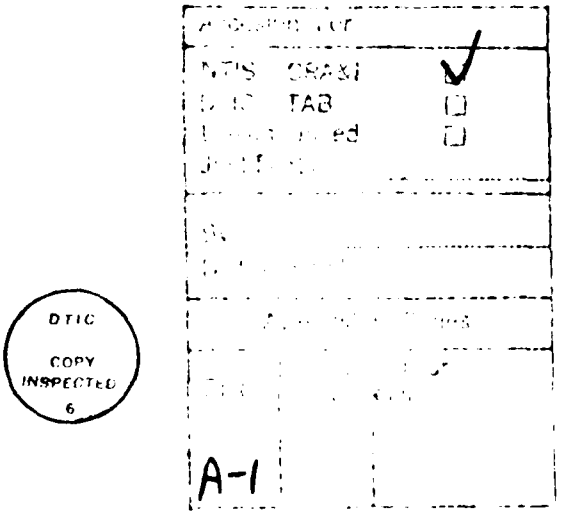

* Research supported by the National Aeronautics and Space Administration under contract No. NAS1-18107 while resident at the Institute for Computer Applications in Science and Engineering (ICASE), NASA Langley Research Center, Hampton, VA 23665.

I. Introduction

Spectral multigrid methods [9,13,17,18] combine the accuracy of spectral discretizations with the efficiency and flexibility of multigrid solution techniques. To date they have been implemented in an exclusively two-dimensional setting, with applications to elliptic model problems [9,17,18] and to compressible, potential flows [13]. In this paper, spectral multigrid methods are extended to three-dimensional periodic problems and applied to the large-eddy simulation of turbulent flow. This work represents one realization of the prospective large-scale applications of spectral multigrid methods that were discussed in [19].

In section 2, the concept of large-eddy simulation is introduced and the discretized Helmholtz equations are formulated. Section 3 discusses several multigrid algorithms suitable for Poisson and Helmholtz equations. Numerical results on the model problems are discussed in section 4. Finally, the multigrid algorithms developed in the previous sections are incorporated into the full time-dependent turbulence simulation. Numerical results are given in section 5.

II. Incompressible homogeneous turbulence

Large-eddy simulation (LES) models the small spatial scales of a turbulent flow as a function of the large scale variables [2,5,10,11,12,15]. A spatial filter applied to the velocities produces the large-scale velocities from which the small spatial scales have been removed. The validity of LES rests on the assumption that the small scale statistics are insensitive to geometry away from solid boundaries. Inasmuch as this criterion is satisfied, a good LES model is applicable to a wide variety of configurations. Alternatively, the Reynolds averaged Navier-Stokes equations result from time averaging the Navier-Stokes equations [14]. The resulting perturbation velocities, the difference between the true velocities and the averaged velocities, become the velocity fluctuations in time and contain information at all spatial scale lengths. Consequently, Reynolds averaged turbulent models are expected to be more geometry dependent than LES models.

In non-dimensional form, the conventional Navier-Stokes equations are given by

$$\frac{\partial \vec{v}}{\partial t} + \nabla \cdot (\vec{v}\vec{v}) = -\nabla p + \nabla \cdot \nu \nabla \vec{v} \tag{1}$$

$$\nabla \cdot \vec{v} = 0 \tag{2}$$

where $\vec{v}$ is the velocity vector, p is the static pressure, and ν, the kinematic viscosity, is assumed to be constant.

Any flow variable $\mathcal{F}$ can be spatially filtered in the following manner:

$$\overline{\mathcal{F}}(\mathbf{x}) = \int_D G(\mathbf{x} - \mathbf{z}, \Delta)\mathcal{F}(\mathbf{z})d^3z \tag{3}$$

where G is a filter function, Δ is the computational mesh size, and D is the domain of the fluid. It follows that Eq. (3) substantially reduces the amplitude of the high-frequency spatial Fourier components of any flow variable $\mathcal{f}$. Consequently, $\overline{\mathcal{f}}$ can be more accurately termed the large-scale part of $\mathcal{f}$.

The turbulent fields are decomposed into their large and small scale components based on the prescription

$$\mathcal{f} = \overline{\mathcal{f}} + \mathcal{f}' \tag{4}$$

where $\mathcal{f}'$ is the velocity representative of the small spatial scales. The direct filtering of the momentum equation yields

$$\frac{\partial \overline{\vec{v}}}{\partial t} + \nabla\cdot(\overline{\vec{v}}\overline{\vec{v}}) = -\nabla\overline{p} + \nabla\cdot\nu\nabla\overline{\vec{v}} + \nabla\cdot\tau \tag{5}$$

$$\nabla\cdot\overline{\vec{v}} = 0 \tag{6}$$

where

$$\tau_{kl} = -(\overline{\overline{v}_k\overline{v}_l} - \overline{v}_k\overline{v}_l + \overline{v'_k\overline{v}_l} + \overline{\overline{v}_k v'_l} + \overline{v'_k v'_l}) \tag{7}$$

is the subgrid-scale stress tensor. This tensor can be decomposed into

$$L_{kl} = -(\overline{\overline{v}_k\overline{v}_l} - \overline{v}_k\overline{v}_l) \tag{8}$$

$$C_{kl} = -(\overline{v'_k\overline{v}_l} + \overline{v'_l\overline{v}_k}) \tag{9}$$

$$R_{kl} = -\overline{v'_k v'_l} \tag{10}$$

which are respectively, the subgrid-scale Leonard, cross, and Reynolds stresses [6].

The deviatoric, i.e. trace-free, part of the subgrid-scale Reynolds stress tensor, ${}_D\mathbf{R}$, is approximated by the Smagorinsky model

$${}_DR_{kl} = \nu_E\ {}_D\overline{S}_{kl} \tag{11}$$

where ν_E is the velocity dependent eddy viscosity

$$\nu_E(\vec{v}) = 2C_R\,\Delta^2 II_{\overline{S}}^{1/2} \tag{12}$$

with

$$\overline{S}_{kl} = \frac{1}{2}(\frac{\partial\overline{v}_k}{\partial x_l} + \frac{\partial\overline{v}_l}{\partial x_k}) \tag{13}$$

$$II_{\overline{S}} = \overline{S}_{mn}\overline{S}_{mn} \tag{14}$$

(i.e., $\overline{\mathbf{S}}$ is the Favre filtered rate of strain tensor while $II_{\overline{S}}$ is its second invariant) and C_R is the Smagorinsky constant (the Einstein summation convention for repeated indices is assumed.) The cross and Leonard subgrid-scale stresses are approximated with the Bardina model [1]. Together with the subgrid-scale Reynold stresses, one obtains the linear combination model [1]

$$\tau_{kl} = -{}_D(\overline{\overline{v}_k\overline{v}_l} - \overline{\overline{v}}_k\overline{\overline{v}}_l) + \nu_E\ {}_D\overline{S}_{kl}). \tag{15}$$

For purposes of numerical computation, the subgrid-scale stresses are partitioned into the subgrid-scale Reynolds stress and the remaining terms. The latter terms contain no derivatives of velocity, and are therefore treated explicitly along with the advection term.

Substitution of the subgrid-scale stress (15) into Eq. (1) transforms the momentum equation into

$$\frac{\partial \overline{\vec{v}}}{\partial t} + \nabla\cdot(\overline{\vec{v}}\overline{\vec{v}}) = -\nabla\overline{P} + \nabla\cdot(\nu + \nu_E)\nabla\overline{\vec{v}} + \nabla\cdot(\mathbf{L} + \mathbf{C}) \tag{16}$$

where the isotropic components of the total subgrid-scale stress have been lumped together with the pressure to produce a new pressure variable, $\overline{P}$, defined by

$$\overline{P} = p + {}_I L_{kk} + {}_I C_{kk} + {}_I R_{kk}. \tag{17}$$

The subscript I indicates that only the trace of the tensor is considered.

For the isotropic turbulence problem, equations (16) and (6) are solved in a cubic computational domain, periodic in all three spatial directions. Fourier spectral methods are an established approach to this problem [10,12]. The solution is obtained in two steps. In the first step, the convective terms and the Leonard and cross subgrid-scale stresses are solved explicitly while the viscous terms are treated with an implicit algorithm. In the second step, a Poisson equation is solved for the pressure to insure that the velocity field remains divergence-free. For convenience, the overbars are removed hereafter from the primitive variables, and it is understood that the variables refer to spatially averaged quantities. For a first-order time discretization, the first step thus solves

$$\vec{v}^{n*} = \vec{v}^{n} - \Delta t[\vec{\omega}\times\vec{v} + \nabla\cdot({}_D\mathbf{L} + {}_D\mathbf{C})]^n + \Delta t\nabla\cdot(\nu + \nu_E)\nabla\vec{v}^{n*}. \tag{18}$$

Note that the momentum equation is used in rotation form. The pressure therefore acquires the additional term $1/2|\vec{v}|^2$. As a result of the first step, one obtains an intermediate velocity field $\vec{v}^{n*}$ which serves as initial conditions for the correction stage

$$\vec{v}^{n+1} = \vec{v}^{n*} - \Delta t\,\nabla P^{n+1} \tag{19}$$

$$\nabla\cdot\vec{v}^{n+1} = 0 \tag{20}$$

For spectral collocation algorithms, a direct solution of Eq. (18) is not feasible because the matrices, which represent the diffusion operators, are full. The alternative which is discussed here is to use iterative methods, and in particular spectral multigrid (SMG) methods, for the solution. The second step in the splitting algorithm can be transformed into a Poisson equation with constant coefficients which is solved exactly in Fourier space. In practice, both the explicit terms are solved with a third order Runga-Kutta algorithm, while the implicit diffusion terms are approximated with a Crank-Nicholson scheme. The implicit equations are solved at each of the three Runga-Kutta stages.

III. Spectral Representation

When the solution to a numerical problem is approximated by a truncated series of appropriate global basis functions, the solution is said to have a spectral representation. The method of projecting the solution onto the basis function space determines the type of spectral approximation: Galerkin, tau or collocation. Spectral methods are explained thoroughly in [4,9] and a summary of their applications to fluid dynamics is provided in [7]. In this paper, only collocation methods are considered, since they are better suited to the solution of non-linear and variable coefficient problems. Periodicity further restricts us to a Fourier representation of the primitive variables.

Consider the three dimensional periodic function $u(\vec{r})$ on the domain $[0,2\pi]^3$ and its truncated Fourier representation

$$u^{N_x,N_y,N_z}(\vec{r}) = \sum_{k_x=-N_x/2+1}^{N_x/2} \sum_{k_y=-N_y/2+1}^{N_y/2} \sum_{k_z=-N_z/2+1}^{N_z/2} \hat{u}_{k_x,k_y,k_z} e^{i(k_x x+k_y y+k_z z)}. \tag{21}$$

The superscripts on u, henceforth omitted, refer to the set of collocation points

$$\Omega_h = (x_j, y_k, z_l) = (jh_x, kh_y, lh_z), \quad 0 \le j < N_x, 0 \le k < N_y, 0 \le l < N_z. \tag{22}$$

where $h = (h_x, h_y, h_z) = (2\pi/N_x, 2\pi/N_y, 2\pi/N_z)$. The number of collocation points in the x, y, z directions are respectively (N_x, N_y, N_z). To insure spectral accuracy, $u(\vec{r})$ must be a C^∞ function. The function u, evaluated at the collocation points m, n, p, and the Fourier coefficients $\hat{u}_{k_x,k_y,k_z}$ are related through the pair of discrete Fourier transforms

$$u_{m,n,p} = \sum_{k_x=-N_x/2+1}^{N_x/2} \sum_{k_y=-N_y/2+1}^{N_y/2} \sum_{k_z=-N_z/2+1}^{N_z/2} \hat{u}_{k_x,k_y,k_z} e^{i(k_x x_m+k_y y_n+k_z z_p)}. \tag{23}$$

$$\hat{u}_{k_x,k_y,k_z} = \frac{1}{N_x N_y N_z} \sum_{m=0}^{N_x} \sum_{n=0}^{N_y} \sum_{p=0}^{N_z} u_{m,n,p} e^{-i(k_x x_m+k_y y_n+k_z z_p)}. \tag{24}$$

First and second derivatives of u are simply obtained by differentiating Eq. (21) term by term and evaluating the result at the collocation points. For example, the first and second derivatives in the x-direction are

$$\left.\frac{\partial u}{\partial x}\right|_{m,n,p} = \sum_{k_x=-N_x/2+1}^{N_x/2} \sum_{k_y=-N_y/2+1}^{N_y/2} \sum_{k_z=-N_z/2+1}^{N_z/2} ik_x \hat{u}_{k_x,k_y,k_z} e^{i(k_x x_m+k_y y_n+k_z z_p)} \tag{25}$$

and

$$\left.\frac{\partial^2 u}{\partial x^2}\right|_{m,n,p} = \sum_{k_x=-N_x/2+1}^{N_x/2} \sum_{k_y=-N_y/2+1}^{N_y/2} \sum_{k_z=-N_z/2+1}^{N_z/2} (-k_x^2) \hat{u}_{k_x,k_y,k_z} e^{i(k_x x_m+k_y y_n+k_z z_p)}. \tag{26}$$

Derivatives in the y and z directions have similar expressions. When evaluating first derivatives, the highest mode in the direction the derivative (the $N/2$ mode) is removed since it makes a purely imaginary contribution to the first derivative at the collocation points.

In many problems, one is required to solve large systems of equations on fine grids. However, direct methods are often impractical because of the size of the problem, and standard iterative methods have very slow convergence rates. Typically, the high frequency components of the error damp out quickly, while there is a very slow decay of the error on the larger scale lengths. Such relaxation schemes smooth out the error very quickly. Multigrid methods accelerate the convergence of iterative methods by recognizing that low frequency errors on a fine grid become high frequency errors on a coarse grid. Therefore, the smoothed residual is interpolated onto a coarser grid, and a new set of equations, similar to the original set, is solved. The coarsening process is continued until a sufficiently coarse grid is reached on which a direct solution procedure is relatively inexpensive. From the coarsest grid solution, the solution on the next finer grid is obtained by prolongation of the coarse grid correction onto the next finer grid, optionally followed by several relaxation sweeps to eliminate the high frequency errors introduced by the interpolation process. In general, therefore, multigrid algorithms have three components: a restriction operator to transfer residual information from the finer to coarser grids, a prolongation operator to extend a coarse grid correction to the next finer level, and a smoothing algorithm whose objective is to reduce the high frequency components on a given level. There exists an extensive literature on multigrid algorithms. Several good review papers appear in [8].

Spectral multigrid distinguishes itself from other types of multigrid approaches in the choice of the interpolation and prolongation operators. In the problem considered here, all functions are periodic. This leads to the preferred truncated Fourier series representation. Following [17], interpolation of a variable from a fine to coarse grid consists of the following steps. Transform the variable to Fourier space, reject the highest modes not resolvable on the coarse grid, and transform back to physical space on the coarse grid. Prolongation is done in a similarly straightforward manner. After transforming the variable to Fourier space, additional terms are added to the Fourier series with zero coefficients. The newly defined function is then transformed back to physical space on the fine grid. Contrary to the more popular interpolation methods used in the finite-difference context, which always introduce high frequency components into the solution, the spectral interpolation just described is exact for solutions to the constant coefficient Helmholtz equation.

Fast Fourier transform (FFT) methods permit the basic interpolation calculations to be performed in $O(N^3 \log N)$ floating point operations, when the number of nodes in all three directions is equal $N_x = N_y = N_z = N$. The grid transfer operators and the residual calculation are both based on FFT's, the former to interpolate variables between different grids, and the latter to perform first and second derivative evaluations at the grid points. Therefore the overall multigrid scheme has an operation count proportional to $O(N^3 \log N)$.

A. *Relaxation Scheme*

The use of FFT's to calculate the residual restricts the choice of relaxation schemes to simultaneous relaxation schemes such as Jacobi and Richardson. These relaxation schemes are implemented in physical space. Consider the constant coefficient scalar Poisson equation

$$\nabla^2 u = f(\vec{r}). \tag{27}$$

The Richardson scheme is one of the simplest smoothers. Applied to Eq. (27), the solution after one smoothing step becomes

$$u \leftarrow u - \omega r, \tag{28}$$

where r is the residual $f - \nabla^2 u$ and ω is the relaxation parameter. Both stationary (fixed ω) and non-stationary (variable ω) are considered. Equation (28) admits a Fourier analysis. If a single three-dimensional Fourier mode (j, k, l) is substituted into Eq. (27), the smoothing rate, μ, becomes

$$\mu(\theta) = |1 - \omega(k_x^2 + k_y^2 + k_z^2)| \tag{29}$$

where ω is the relaxation parameter. In the context of multigrid methods, the objective is to minimize the smoothing rate of the high frequencies seen by the fine grid, and not resolvable on the coarser ones. Given an existing grid, the next level of coarsening is obtained by defining the set of collocation points Ω_{2h}. The range of wavenumbers over which the minimization is performed is the difference between the two cubes (in wave number space) $[0, \frac{N}{2}]^3$ and $[0, \frac{N}{4}]^3$. Strictly speaking, because both the mean mode and the $N/2$ mode have been filtered out of the right hand side, $f(\vec{r})$, the wave numbers considered for the minimization should actually be in the region defined by the difference between the cubes $[1, \frac{N}{2}]^3$ and $[1, \frac{N}{4}]^3$.

A straightforward calculation leads to an optimal smoothing rate of

$$\overline{\mu} = \frac{N_d - \frac{1}{4}}{N_d + \frac{1}{4}} \tag{30}$$

for the Richardson iteration scheme, where N_d is the number of spatial dimensions. When $N_d = 3$, $\overline{\mu} = 11/13 \approx .85$. It is obvious from Eq. (30) that the asymptotic smoothing rate increases with increasing spatial dimension. For example, as the number of dimensions increases from 1 to 3, $\overline{\mu}$ increases from 0.6 to 0.85. For 3-D problems, the optimal relaxation parameter is

$$\omega = \frac{32}{13N^2} \tag{31}$$

Operators that are spectrally discretized have a wider spread of eigenvalues than their finite-difference counterparts. For example, the optimal Richardson smoothing rate for a second-order, central difference discretization of the constant coefficient Poisson equation is

$$\overline{\mu}_{FD} = \frac{N_d - \frac{1}{2}}{N_d + \frac{1}{2}} \tag{32}$$

In contrast to the spectral smoothing rates, $\overline{\mu}_{FD}$ ranges from 0.33 to 0.71 for 1, 2 and 3-D problems.

Brandt, Fulton and Taylor [3] applied the residual averaging technique to accelerate the convergence of Richardson's smoothing algorithm for two-dimensional Fourier representations. The extension to the present three-dimensional problem is straightforward. The smoothing algorithm now satisfies

$$u_{mnp} = u_{mnp} - \frac{4\pi^2}{N^2} A r_{mnp} \tag{33}$$

where (m, n, p) is the grid point to which the smoother is applied and A is the averaging template. A is the three-dimensional array

$$A = \begin{pmatrix} \delta & \gamma & \delta \\ \gamma & \beta & \gamma \\ \delta & \gamma & \delta \end{pmatrix}, \begin{pmatrix} \gamma & \beta & \gamma \\ \beta & \alpha & \beta \\ \gamma & \beta & \gamma \end{pmatrix}, \begin{pmatrix} \delta & \gamma & \delta \\ \gamma & \beta & \gamma \\ \delta & \gamma & \delta \end{pmatrix}. \tag{34}$$

If elements of A are denoted by A_{ijk}, the three arrays in the above expression correspond (from left to right) to $k = 1, 2, 3$. The parameter δ is associated with the 8 corner points of the cube centered at (m, n, p) about which the averaging is being performed. In conventional notation, the averaging template A applied to the residual at (m, n, p) produces the expression

$$A r_{m,n,p} = [\alpha + \beta \sum_{|i|+|j|+|k|=1} + \gamma \sum_{|i|+|j|+|k|=2} + \delta \sum_{|i|+|j|+|k|=3}] r_{m+i,n+j,p+k}. \tag{35}$$

Such a scheme is called weighted residual averaging (WRA). A Fourier analysis applied to Eq. (33) yields

$$\begin{aligned} \mu(k_x, k_y, k_z; \alpha, \beta, \gamma, \delta) \;=\; & |1 - \frac{4\pi}{N^2}(k_x^2 + k_y^2 + k_z^2)[\alpha + 2\beta(\cos\theta_x + \cos\theta_y + \cos\theta_z) \\ & + 4\gamma(\cos\theta_y \cos\theta_x + \cos\theta_z \cos\theta_z + \cos\theta_x \cos\theta_y) \\ & + 8\delta(\cos\theta_x \cos\theta_y \cos\theta_z)]|. \end{aligned} \tag{36}$$

where $(\theta_x, \theta_y, \theta_z)$ is a shorthand notation for $\frac{2\pi}{N}(k_x, k_y, k_z)$. The solution to the minimax problem

$$\overline{\mu} = \min_{\alpha,\beta,\gamma,\delta} \max_{\theta_x,\theta_y,\theta_z} \mu(\theta_x, \theta_y, \theta_z; \alpha, \beta, \gamma, \delta) \tag{37}$$

yields the optimum parameters α,β,γ, and δ as well as the smoothing rate $\overline{\mu}$. This is solved numerically. The angles lie in the region formed by the difference between the two cubes $[0, \pi/2]^3$ and $[0, \pi/4]^3$. To demonstrate the importance of all four averaging coefficients, $\overline{\mu}$ was calculated by successively increasing the number of non-zero coefficients. The results are presented in table 1 where a comparison is made with the 2-D results of Brandt, Fulton and Taylor [3]. In both 2-D and 3-D, $\overline{\mu}$ decreases substantially with the help of residual averaging. As expected, the minimum 3-D spectral radius is higher than the optimal 2-D value.

α	β	γ	δ	3-D $\overline{\mu}$	2-D $\overline{\mu}$
0.062	0.000	0.0	0.0	0.852	0.777
0.101	0.145	0.0	0.0	0.608	0.472
0.120	0.287	0.0083	0.0	0.453	0.106
0.144	0.042	0.0185	0.0085	0.195	–

Table 1: Optimal averaging parameters and smoothing rates for weighed residual averaging scheme.

B. Variable Coefficient Poisson Equation

The analysis of the previous section is exact for the constant coefficient Poisson equation. More generally, one wishes to solve

$$\nabla \cdot a(\vec{r}) \nabla u = f(\vec{r}) \tag{38}$$

where $a(\vec{r})$ is a strictly positive C^∞ function. Although convergence is no longer theoretically guaranteed, good results are obtained if the residual is first divided by $a(\vec{r})$ before averaging. Alternatively, one can use Eq. (33) after replacing $4\pi^2/N^2$ by $4\pi^2/a(\vec{r})N^2$. Both approaches yield similar results. The results presented herein are based on the former method.

C. Helmholtz Equation

With the good convergence rates achieved for the Poisson equation, attention is now focussed on the three-dimensional Helmholtz equation

$$\nabla \cdot a \nabla u - \Lambda u = f(\vec{r}) \tag{39}$$

where $a(\vec{r})$ is a C^∞ function and Λ is a positive constant. The iteration scheme and its associated convergence rate are respectively

$$u \leftarrow u - \omega \left(f(\vec{r}) - \nabla \cdot a \nabla u + \Lambda u \right) \tag{40}$$

and

$$\mu = |1 - \omega(k^2 + \Lambda)| \tag{41}$$

where, as previously, the number of grid points is assumed to be equal in all directions ($N_x = N_y = N_z = N$). The optimum smoothing rate is

$$\overline{\mu} = \frac{11/13}{1 + \dfrac{32}{13N^2} \dfrac{\Lambda}{a}} \tag{42}$$

which is exact for constant coefficient a. (It is assumed that the $k_x = k_y = k_z = 0$ mode is solved for exactly on the coarsest grid.) Note that the difference in smoothing rates of the Poisson and Helmholtz operators decreases with increasing grid size.

Experiments were also performed with a non-stationary Richardson smoothing algorithm. If κ is the condition number

$$\kappa = \frac{\lambda_{max}}{\lambda_{min}} \tag{43}$$

of the discrete spectral operator $\nabla \cdot a\nabla - \Lambda$, the j^{th} relaxation parameter, ω_j^k of a k-parameter cycle is

$$\omega_j^k = \frac{2/\lambda_{min}}{(\kappa - 1)\cos(\frac{(2j-1)\pi}{2k}) + (\kappa + 1)} \qquad j = 1, ..., k \tag{44}$$

and the corresponding smoothing rate is

$$\overline{\mu}_j = T_j \left(\frac{\kappa + 1}{\kappa - 1}\right)^{-1/j} \tag{45}$$

which is the solution to a standard minimax problem [16]. The range of frequencies that are preferentially damped are in the domain defined by the difference between the two cubes $[0, \lambda_{max}]^3$ and $[0, \lambda_{min}]^3$. As a function of Λ and of the coefficient $a(\vec{r})$, the minimum and maximum eigenvalues of the discrete Helmholtz operator are

$$\lambda_{min} = \frac{aN^2}{16} + \Lambda, \qquad \lambda_{max} = \frac{3aN^2}{4} + \Lambda \tag{46}$$

and the sequence of optimal relaxation parameters in the non-stationary Richardson iteration scheme become

$$\omega_j^k = \frac{32}{aN^2 + 16\Lambda} \frac{1}{(\kappa - 1)\cos(\frac{\pi(2j-1)}{2k}) + (\kappa + 1)}. \tag{47}$$

The number of terms in the sequence is set equal to the number of smoothing sweeps. For stationary Richardson, $j = 1$ and Eqs. (47) reduces to

$$\omega = \frac{\frac{32}{13N^2}}{1 + \frac{32}{13N^2}\frac{\Lambda}{a}} \tag{48}$$

while $\overline{\mu}$ is given by Eq. (42) If the value of λ_{min} and λ_{max} (Eq. (46) are inserted into the condition number defined by Eq. (43), it is clear that the convergence rate must increase when either N, or Λ is increased.

Table 2 confirms that $\overline{\mu}$ decreases with increasing Λ and j. In practice, a 3-cycle scheme is sufficient to reduce the L_2 norm of the residual by a factor of 5. An alternate formulation of the Richardson method is obtained when the Helmholtz term is treated implicitly, i.e

$$u \leftarrow \frac{u - \omega_P(f(\vec{r}) - \nabla \cdot a\nabla u)}{1 + \Lambda\omega_P} \tag{49}$$

or equivalently

$$u \leftarrow u + \omega_H(f(\vec{r}) - \nabla \cdot a \nabla u) \tag{50}$$

where ω_H is the implicit Helmholtz relaxation parameter

$$\omega_H = \frac{\omega_P}{1 + \Lambda \omega_P}. \tag{51}$$

If ω_P is the optimum relaxation parameter for the constant coefficient Poisson operator, given by

$$\omega_P = \frac{32}{13N^2 a}, \tag{52}$$

ω_H is identical to the value obtained in Eq. (48). Therefore the two algorithms are identical for all $a > 0$. However they differ from one another for non-stationary Richardson. Indeed, in the implicit formulation, one chooses the ω_j^k to optimize the convergence of the Poisson operator which leads to relaxation parameters independent of Λ. The Λ dependence is introduced as an extra positive term in the denominator of Eq. (49). This is in contrast to w_j^k given by Eq. (47) where Λ appears in the coefficient of the cosine function. Table 3 illustrates the differences between the two approaches when non-stationary Richardson is used with cycles of varying length. The two methods give approximately identical smoothing rates, except in the limit of large Λ where the implicit method gives slightly better performance. From a practical point of view, it is cheaper to evaluate the acceleration parameters for the implicit scheme because a factor $1/a$ can be factored out of ω_j^k and combined with the residual. This is not possible for the explicit formulas which depend on $\vec{r}$.

k	$\overline{\mu}(\Lambda = 0)$	$\overline{\mu}(\Lambda = 10)$	$\overline{\mu}(\Lambda = 50)$
1	0.846	0.826	0.755
2	0.747	0.720	0.631
3	0.689	0.661	0.573
4	0.655	0.628	0.542
5	0.634	0.607	0.524
6	0.619	0.593	0.512

Table 2: Smoothing rates for non-stationary Richardson iteration applied to the Helmholtz equation.

D. Implementation

The stationary and non-stationary relaxation schemes were implemented in a simple V-cycle formulation which is described in detail in [17,18] for the two-dimensional Poisson

		Grid Size		
		32^3	64^3	128^3
	1	0.652/0.651	0.654/0.654	0.655/0.655
Λ	10	0.628/0.618	0.648/0.645	0.653/0.653
	50	0.542/0.511	0.621/0.610	0.646/0.643

Table 3: Comparison of convergence rates of explicit versus implicit non-stationary Richardson iteration algorithms.

equation. Results are based on a fine grid of 32^3 and 3 coarser grids of 16^3, 8^3 and 4^3. A constant number of relaxation sweeps on each grid on the upwards (N_u) and downward (N_d) branches of the V-cycle was found to provide good overall smoothing rates for all the cases that were considered. An effective rule of thumb is to decrease the residual by an order of magnitude on each grid. This leads to $N_d = 2$ for WRA, because of the high smoothing rates, and $N_d = 3$ for the non-stationary Richardson (NSR) schemes. This corresponds to an approximate decrease of the L_2 norm of the residual on the order of 0.2 and 0.05 for the WRA and NSR respectively (per N_d fine grid relaxations). In all tests, $N_u = 1$. This is because the variable coefficient a introduces high frequencies into the residual after a prolongation.

All the computations presented were performed on the Cray 2. Fast Fourier transforms are coded in Fortran, and achieve a 100 Mflop rate on grids on 64^3 and above. Timings may fluctuate by $10\% - 20\%$ for identical runs due to system load.

E. Results

There are many different approaches to measuring the efficiency of a multigrid algorithm. Ultimately, the user is interested in the total CPU clock time a code takes to complete execution. However, this timing is strongly computer dependent, and on a given system, the programmers skill can greatly influence the results. It is therefore necessary to supplement the CPU time with more intrinsic measures. The simplest measure is the smoothing rate $\overline{\mu}$ of the smoother on the finest grid. Unfortunately, $\overline{\mu}$ does not take into account the work done on the coarser grids, nor does it account for the time spent performing grid transfers. Alternate criteria are required to take this work into account. One method is to calculate the ratio of L_2 norms of the residual after and before a single V-cycle, and calculate a smoothing rate per V-cycle as

$$\overline{\mu}_V = \left(\frac{||r_{exit}||}{||r_{entry}||} \right)^{1/N_f} \tag{53}$$

where N_f is the total number of fine grid sweeps during one V-cycle ($N_u + N_d$). Although $\overline{\mu}_V$ is still not useful as an accurate measure of efficiency since it does not take residual transfers into account, it can help establish whether the high frequencies seen by each grid are damped at the same rate. If $\overline{\mu}$ and $\overline{\mu}_V$ are unequal and the number of relaxations is the same on every grid (except perhaps the coarsest), the frequency content of the error vector is unevenly distributed, and the smoothing rates will be different on each grid. Therefore, $\overline{\mu}_V$ is useful as a diagnostic tool.

A better measure of the overall algorithm efficiency is obtained from the number of equivalent fine relaxation sweeps defined as

$$N_{eq} = \frac{CPU\ time\ per\ V-cycle}{CPU\ time\ per\ fine\ grid\ relaxation}. \tag{54}$$

The equivalent convergence rate

$$\overline{\mu}_T = \left(\frac{||r_{exit}||}{||r_{entry}||} \right)^{1/N_{eq}} \tag{55}$$

measures the decrease in the residual norm per fine sweep taking the total multigrid overhead into account. Together with the total CPU time per V-cycle, the performance of the algorithm can be ascertained. In what follows, performance is measured exclusively by $\overline{\mu}$ and $\overline{\mu}_T$. Processing time is a function of the number of relaxation sweeps on the way up and down the V-cycle, and on the grid size. These parameters are kept constant within a given table except in table 6 where the effect of fine-grid resolution is studied. Therefore, the decrease in the residual norm after a fixed number of multigrid cycles is an objective measure of the algorithm's efficiency.

As explained in detail in [18], the $N/2$ Fourier mode must be filtered out of the residual every time it is computed. In one dimension, this is done in physical space by projecting the residual function onto the space orthogonal to $(-1)^j, j = 1, N_x$. In higher dimensions, a sequence of 1-D filtering operations is performed. The filtering operation consumes approximately 25% of the residual calculation on a 32^3 grid. The influence of vectorization is clearly seen from the decrease in relative time spent filtering as the grid size increases. For example, as N increases from 32 to 128, the percentage of time spent filtering, measured with respect to the total time spent calculating the residuals (which includes the filtering), decreases from 25% to 13%. Equivalently, the percentage of time spent in 3-D derivative evaluations during the computation of the residual increases from 67% to 77% as the grid size increases from 32^3 to 128^3.

When solving the Poisson equation, the mean value of the right-hand side of the equation must be filtered out to insure convergence of the residual towards zero [18]. This is done once at the beginning of the calculation.

All the numerical experiments were done with the Helmholtz equation (with Λ set to a constant value). The Poisson equation is obtained by setting Λ to zero. The coefficient

$a(\vec{r})$ is set to

$$a(\vec{r}) = 1 + \epsilon e^{\cos(x)+\cos(y)+\cos(z)}, \tag{56}$$

In all cases considered, the right hand side of the Helmholtz equation is calculated to insure that the exact solution is

$$u_{ex}(\vec{r}) = \sin(N_x \pi \sin(x)) \sin(N_y \pi \sin(y)) \sin(N_z \pi \sin(z)) \tag{57}$$

The factors N_x, N_y and N_z are included to insure that the complete spectrum of spatial scales are equally represented in the error vector. This insures that $\overline{\mu} = \overline{\mu}_V$. Such a solution however, precludes a direct comparison of the computed and the exact solution because u_{ex} is no longer well represented by the collection of Fourier modes.

Convergence results for the WRA are presented in table 4. The smoothing rates obtained for the constant coefficient Poisson equation are lower than the theoretical predictions. This is mainly because the analytic results presented in Table 1 are only valid in the limit $N \to \infty$. Although $a(\vec{r})$ varies by a factor 20 across the physical domain when $\epsilon = 1$, $\overline{\mu}$ remains close to the optimal value of 0.2. Experiments have shown that a large degradation of $\overline{\mu}$ occurs for ϵ greater than 1.5. Seven V-cycles reduced the residual 10 to 11 orders of magnitude. Timings indicate that the number of equivalent fine relaxations is 3.45 on a 32^3 grid. This is larger than is expected from the sum of the work done on the sequence of grids obtained from summing the geometric series $1 + (\frac{1}{2})^3 + (\frac{1}{8})^3 + (\frac{1}{64})^3 + \cdots$

ϵ	0.0	0.5	1.0
$\overline{\mu}$	0.17	0.18	0.19
$\overline{\mu}_T$	0.61	0.58	0.61
$\frac{\|r_7\|}{\|r_1\|}$	4(-11)	3(-10)	1(-10)

Table 4: Rates of convergence for Poisson equation

which leads to 1.13 equivalent work units. The discrepancy between the theoretical and numerical results are due to the time spent in the grid transfers which are not included in the geometric series, and the inefficiency of the Cray 2 program on the coarser grids.

Large eddy simulations of turbulence require that the numerical scheme be capable of resolving a wide range of spatial scale lengths. Furthermore, the velocity fields have a quasi-random distribution over the set of scale-lengths that survive the the filtering. In typical large eddy simulations, the smallest fluctuations seen by the LES code are on the order of 4 fine grid cell widths (albeit with small amplitudes). It is therefore important to ascertain the influence of spatial structure in $a(\vec{r})$ on the smoothing rate of the Poisson and Helmholtz operators. To this effect, the definition of the coefficient $a(\vec{r})$ is slightly

modified according to

$$a(\vec{r}) = 1 + \epsilon e^{\cos(n_\epsilon x)+\cos(n_\epsilon y)+\cos(n_\epsilon z)}. \tag{58}$$

With $\epsilon = 0.5$, a varies from 1 to about 10. The influence of n_ϵ is to introduce high frequency content into the coefficient without affecting its range. In other words, the higher n_ϵ, the smaller the distance over which a assumes its maximum variation. Table 5 shows that small values of n_ϵ do not adversely affect the convergence rate of the iteration scheme.

n_ϵ	$\overline{\mu}$	$\overline{\mu}_V$
1	0.17	0.17
2	0.18	0.18
4	0.55	0.55
8	0.58	0.62

Table 5: Effect of high frequency content of a($\vec{r}$) on the smoothing rate

However, the rate of convergence rate quickly deteriorates for $n_\epsilon \geq 4$. Note that when the variation of a becomes too rapid, there is a discrepancy between $\overline{\mu}$ and $\overline{\mu}_V$. This probably indicates that there is a frequency imbalance across the various grid levels, due to the grid transfer operators which do not properly interpolate $a(\vec{r})$ onto the coarser grids. Similar experiments performed on the Helmholtz equation indicate that Λ has a beneficial effect on the smoothing rate as n_ϵ is increased. Of course, $\overline{\mu}$ is higher than the worst Poisson result since residual averaging is not allowed.

The Helmholtz equation is numerically solved for several values of ϵ and Λ. Non-stationary Richardson with a cycle of 3 produces the results displayed in table 6. Pairs of numbers correspond to ($\epsilon = 0/\epsilon = 0.5$). As expected, for a fixed ϵ, $\overline{\mu}$ decreases with increasing Λ due to the reduction of the condition number

$$\kappa = \frac{\lambda_{max}}{\lambda_{min}} \tag{59}$$

$$= \frac{\frac{1}{16}aN^2 + \Lambda}{\frac{3}{4}aN^2 + \Lambda}. \tag{60}$$

For the larger values of Λ, the effect of non-constant coefficient a is more severe. Whereas $\overline{\mu}$ is almost unaffected by ϵ for $\Lambda < 40$, the differences in smoothing rates are substantial for $\Lambda > 100$. For instance, when $\Lambda = 1000$, $\overline{\mu}$ is approximately 3 times larger for $\epsilon = 0.5$ than for $\epsilon = 0.0$. Similar trends occur for $\overline{\mu}_T$. However, the influence of ϵ on $\overline{\mu}_T$ is less dramatic at high Λ.

Λ	1	10	100	1000
$\overline{\mu}$	0.68/0.68	0.66/0.67	0.49/0.62	0.16/0.42
$\overline{\mu}_T$	0.87/0.88	0.86/0.86	0.77/0.83	0.63/0.76
$\frac{r_{10}}{r_1}$	3(-5)/1(-4)	1(-5)/2(-5)	5(-9)/2(-6)	1(-11)/2(-9)

Table 6: Rates of convergence for Helmholtz equation

Optimal multigrid methods produce convergence rates independent of the grid size. This is tested for the Helmholtz equation at $\epsilon = 0.5$ and $\Lambda = 10$. Table 7 indicates that both $\overline{\mu}$ and $\overline{\mu}_T$ are approximately constant over fine grid sizes that range between 32^3 and 128^3. In all cases, the coarsest grid level is 4^3. Computer timings for the calculations are also presented. They are normalized to 1 on the 64^3 grid. In all cases, the code is stopped after a fixed number of V-cycles. Increased time spent on the 128^3 grid relative to the 64^3 agrees quite well with theoretical predictions. This is in contrast to the extra 70% CPU time spent on the 32^3 grid than allowed for by the $O(N \log N)$ scaling. Poor vectorization on this grid is the probable cause of this discrepancy.

grid size	32^3	64^3	128^3
$\overline{\mu}$	0.67	0.67	0.68
$\overline{\mu}_T$	0.86	0.85	0.85
$\frac{r_{10}}{r_1}$	1.9(-5)	1.5(-4)	2.5(-5)
CPU time (arbitrary units)	0.18	1.0	9.0
$O(N^3 \log N)$ (arbitrary units)	0.10	1.0	9.3

Table 7: Grid independence for Helmholtz equation, $\epsilon = 0.5$, $\Lambda = 10$

F. Large Eddy Simulation

The implicit stage of the LES equations requires the solution to the set of three scalar Helmholtz equations given by equation (18). Defining

$$a = \frac{\nu + \nu_E(\vec{v})}{< \nu + \nu_E(\vec{v}) >} \tag{61}$$

$$\Lambda = \frac{2}{< \nu + \nu_E(\vec{v}) > \Delta t}, \tag{62}$$

Equ. (18) reduces to the three scalar Helmholtz equations

$$\nabla \cdot a(\vec{v}) \nabla \vec{v}(\vec{r}) - \Lambda \vec{v} = \vec{v}^*, \tag{63}$$

where $\vec{v}^*$ is the flow velocity after the explicit step. The above definitions of $a(\vec{r})$ and Λ insure that $< a >= 1$, which allows the numerical results to be compared against the results in the previous sections.

A major difficulty expected to reduce the efficiency of the multigrid implementation, when compared with the theoretical and model problem results, is that $a(\vec{r})$ is now, in effect, a random function of the spatial coordinates. Numerical experiments indicate that the multigrid algorithm fails to converge for Λ below a certain threshold. In the current code, this threshold is $\Lambda \approx 100$. Convergence rates and timings are shown in table 8. Calculations were performed on a 32^3 grid.

Although equation (63) has the same functional form as the model equation, the effect of $a(\vec{r})$ and Λ on the overall multigrid efficiency relative to a purely explicit scheme is not easy to determine. One reason is the strong dependence of these parameters on the filter width Δ, kinematic viscosity ν, and Smagorinsky constant C_R. To understand better the interelations between these parameters and the possible gain of a multigrid strategy, let

$$\mathcal{R} = \frac{\Delta t_{diff}}{\Delta t_{adv}} \tag{64}$$

where Δt_{adv} and Δt_{diff} are respectively the maximum time steps calculated for the explicit advection and diffusive terms. The accuracy of the simulation is mostly determined by the advection terms. Implicit algorithms are consequently most favorable when the diffusion time step is much smaller than Δt_{adv} (i.e. when $\mathcal{R} << 1$). Stated differently, a fully explicit solver is cheaper than a mixed explicit/implicit scheme when $\mathcal{R} >> 1$. For Fourier methods, the maximum advection Courant number of the third order Runga-Kutta method is 0.6, which leads to

$$\Delta t_{adv} = 0.6 \frac{\Delta x}{v}. \tag{65}$$

where v is a representative fluid velocity. (The estimates in this section are for a one-dimensional problem.) On the other hand, the diffusion time limit is

$$\Delta t_{diff} = 0.25 \frac{\Delta x^2}{\nu + \nu_E}. \tag{66}$$

In this discussion, all the variables are assumed to be constant. Equations (65) and (66) combine into

$$\mathcal{R} = \frac{v \Delta x}{f(v) C_R n_\Delta^2 \Delta x^2 + \nu}. \tag{67}$$

Several substitutions have been made to arrive at Eq. (67). The filter width Δ has been replaced by $n_\Delta \Delta x$ to separate the computational grid size from the actual filter width.

Thus, when n_Δ is increased, the filtering is stronger, and more high frequencies are removed from the large-eddy velocities. The velocity dependence of the Smagorinsky model is included in $f(v)$ whose magnitude is a slowly decaying function of n_Δ.

As confirmed in table 8, the convergence rate improves with increasing Λ. However, according to Eq. (62), a higher Λ is the result of a decrease in n_Δ, C_R or ν. Other sources of variation are not considered here. Equation (67) therefore clearly indicates that a higher Λ reduces the gain of the multigrid scheme over the purely explicit scheme. This is borne out by table 8. The multigrid code performs 2 times slower than the explicit scheme when $\Lambda = 130$ and 9 times slower when $\Lambda = 1000$ although $\overline{\mu}$ has dropped from 0.58 to 0.12. Furthermore, as Λ increases, so does $\mathcal{R}$ which explains why the multigrid code performs so poorly (compared to the explicit scheme) for large Λ. The variation of the results in the table 8 is not uniformly monotonic as a function of Λ. This is partially because timings are a function of the load on the Cray 2, and of the interaction between the various independent control parameters. For example, if Λ is increased through a smaller value n_Δ, the high frequency content in the velocities is reduced and better SMG convergence rates are expected, not only due to the larger Helmholtz coefficient, but also because of the smoother velocity fields. On the other hand, only the former cause for improvement is remains when C_R is decreased.

Finally, $a(\vec{r})$ was assumed to be constant in the above analysis. In all probability, the oscillatory nature of $a(\vec{r})$ will also strongly influence the performance of the SMG. When Λ drops below 100, the implicit scheme fails to converge. This might be related to the highly oscillatory coefficients which appear when simulating turbulent flows.

		impl. code vs. expl. code	
Λ	$\overline{\mu}$	*time/step*	*time/run*
< 100	non-converged		
130	0.58	16	2
200	0.75	21	2
240	0.26	12	2
480	0.21	10	3
540	0.20	12	4
700	0.20	14	7
1000	0.12	12	9

Table 8: Numerical results from SMG incorporated into the multigrid code. Figures refer to 5 complete time steps.

More efficient Helmholtz solvers must be developed before spectral multigrid algorithms

will strongly outperform the explicit schemes for the simulation of turbulent flows. The quasi-random coefficients in the LES equations also call for new spectral interpolation procedures to improve the robustness of the method.

G. Conclusion

Three dimensional periodic Poisson and Helmholtz equations have been solved with a 3-D spectral multigrid algorithm. Convergence rates for the Poisson problem are best when weighted residual averaging is adopted. The spatially dependent coefficient $a(\vec{r})$ was allowed to vary by more than an order of magnitude without affecting overall convergence rates. Although weighted residual averaging is impractical for the 3-D Helmholtz equation, non-stationary Richardson is a viable alternative for a wide range of a and Λ. At a fixed amplitude variation, high spatial frequency content of a had a deleterious effect on $\overline{\mu}$ for the Poisson equation. This is unfortunate since for turbulent simulations the variables are necessarily oscillatory.

The algorithms herein were successfully incorporated into a full 3-D, non-stationary incompressible LES code. It was found that in the range of parameters examined, the SMG takes at least twice as long as an explicit calculation. This is part due to the relatively large spread of eigenvalues for a Fourier collocation algorithm. Another cause is most probably related to the strong and rapid variations of $a(\vec{r})$.

H. Acknowledgements

The first author would like to thank Duane Melson, Craig Streett and Frank Thames for fruitful discussions which helped him better understand some of the fine points multigrid algorithms.

References

[1] Bardina, J., Ferziger, J. H., & Reynolds, W. C. 1983 Improved Subgrid-Scale Models based on Large-Eddy Simulation of Homogeneous, Incompressible, Turbulent Flows. Stanford Report TF-19.

[2] Biringen, S. & Reynolds, W. C. 1981 Large-Eddy Simulation of the Shear-Free Turbulent Boundary Layer. *J. Fluid Mech.*, **103**, 53-63.

[3] Brandt, A., Fulton, S. R. and Taylor, G. D. 1985 Improved Spectral Multigrid Methods for Elliptic Problems. *J. Comput. Phys.*, **58**, 96-112.

[4] Canuto, C., Hussaini, M. Y., Quarteroni, A. & Zang, T. A., 1987 *Spectral Methods in Fluid Dynamics.* Springer-Verlag.

[5] Clark, R. A., Ferziger, J. H. & Reynolds, W. C. 1979 Evaluation of Subgrid-Scale Models using an Accurately Simulated Turbulent Flow. *J. Fluid Mech.* **91**, 1-16.

[6] Erlebacher, G., Hussaini, M.Y., Speziale, C. G. and Zang, T.A. 1987 Toward the Large-Eddy Simulation of Compressible Turbulent Flows. ICASE Report No. 87-20, NASA Contractor Report 178273.

[7] Gottlieb, D. and Orszag, S. A. 1977 Numerical Analysis of Spectral Methods: Theory and Applications. *Regional Conference Series in Applied Mathematics*

[8] Hackbusch, W. and Trottenberg, U., Ed. *Multigrid Methods*, Proceedings of a Conference (Koln-Porz, Nov. 1981), Springer-Verlag, 1982.

[9] Hussaini, M. Y., & Zang, T. A. 1987 Spectral Methods in Fluid Dynamics. *Ann. Rev. Fluid Mech.* **19**, 339-368.

[10] McMillan, O. J. & Ferziger, J. H. 1979 Direct Testing of Subgrid-Scale Models. *AIAA J.* **17**, 1340-1346.

[11] Reynolds, W. C. 1976 Computation of Turbulent Flows, *Ann. Rev. Fluid Mech.* **8**, 183-208.

[12] Rogallo, R. S. & Moin, P. 1984 Numerical Simulation of Turbulent Flows. *Ann. Rev. Fluid Mech.* **16**, 99-137.

[13] Streett, C. L., Zang, T. A. and Hussaini, M. Y. 1985 Spectral Multigrid Methods with Applications to Transonic Potential Flow, *J. Comput. Phys.* **57**, 43-76.

[14] Tennekes, H. & Lumley, J. L. 1972 *A First Course in Turbulence* MIT press.

[15] Voke, P. R. & Collins, M. W. 1983 Large-Eddy Simulation: Retrospect and Prospect. *PhysicoChemical Hydrodynamics* **4**, No. 2, 119-161.

[16] Young, D. M. 1954 On Richardson's Method for Solving Linear Systems with Positive Definite Matrices, *J. Math. Phys.* **22**, 243-255.

[17] Zang, T. A., Wong, Y. S., and Hussaini, M. Y. 1982, *J. Comput. Phys.* **48**, 485-501.

[18] Zang, T. A., Wong, Y. S., and Hussaini, M. Y. 1982 Spectral Multigrid Methods for Elliptic Equations II. *J. Comput. Phys.* **54**, 489-507.

[19] Zang, T. A. and Hussaini, M. Y. 1986 On Spectral Multigrid Methods for the Time-Dependent Navier-Stokes Equations. *Appl. Math. Comput.* **19**, 359-372.

Standard Bibliographic Page

1. Report No. NASA CR-178341 ICASE Report No. 87-45	2. Government Accession No.	3. Recipient's Catalog No.
4. Title and Subtitle SPECTRAL MULTIGRID METHODS FOR THE SOLUTION OF HOMOGENEOUS TURBULENCE PROBLEMS		5. Report Date July 1987 6. Performing Organization Code
7. Author(s) G. Erlebacher, T. A. Zang, and M. Y. Hussaini		8. Performing Organization Report No. 87-45
9. Performing Organization Name and Address Institute for Computer Applications in Science and Engineering Mail Stop 132C, NASA Langley Research Center Hampton, VA 23665-5225		10. Work Unit No. 505-90-21-01 11. Contract or Grant No. NAS1-18107
12. Sponsoring Agency Name and Address National Aeronautics and Space Administration Washington, D.C. 20546		13. Type of Report and Period Covered Contractor Report 14. Sponsoring Agency Code

15. Supplementary Notes

Langley Technical Monitor:
J. C. South

Submitted to the Proc. of the Third Copper Mountain Conference on Multigrid Methods

Final Report

16. Abstract

New three-dimensional spectral multigrid algorithms are analyzed and implemented to solve the variable coefficient Helmholtz equation. Periodicity is assumed in all three directions which leads to a Fourier collocation representation. Convergence rates are theoretically predicted and confirmed through numerical tests. Residual averaging results in a spectral radius of 0.2 for the variable coefficient Poisson equation. In general, non-stationary Richardson must be used for the Helmholtz equation. The algorithms developed are applied to the large-eddy simulation of incompressible isotropic turbulence.

17. Key Words (Suggested by Authors(s))

Navier-Stokes equations, homogeneous turbulence, spectral collocation, split method

18. Distribution Statement

34 - Fluid Mechanics and Heat Transfer
64 - Numerical Analysis

Unclassified - unlimited

19. Security Classif (of this report)	20. Security Classif (of this page)	21. No. of Pages	22. Price
Unclassified	Unclassified	21	A02

For sale by the National Technical Information Service, Springfield, Virginia 22161

NASA Langley Form 63 (June 1985)

NASA Catalog, 1987

END

DATE

FILMED

MARCH

1988

DTIC